PHYSICS

Manipulating the direction of turbulent energy flux via tensor geometry in a two-dimensional flow

Xinyu Si[1], Filippo De Lillo[2], Guido Boffetta[2], Lei Fang[1,3]*

In turbulent flows, energy flux, the cornerstone of turbulence theory, refers to the transfer of kinetic energy across different scales of motion. The direction of net energy flux is prescribed by the dimensionality of the fluid system: Energy cascades to smaller scales in three-dimensional flows but to larger scales in two-dimensional (2D) flows. Manipulating energy flux is a formidable task because the energy at any scale is not localized in the physical space. Here, we report a theoretical framework that enables control over energy flux direction. On the basis of this framework, we conducted experiments and direct numerical simulations, producing a 2D turbulence with forward energy flux, contrary to classical expectations. Beyond theory, we discuss how our theoretical framework can have profound applications and implications in natural and engineered systems across length scale ranges from 10^{-3} to 10^{6} meters, including enhanced mixing of microfluidic devices, biologically generated turbulence, breaking persistent coastal transport barriers, and ocean energy budget.

INTRODUCTION

Turbulence governs the motion of many fluid systems, including the oceans and atmosphere, and serves as an efficient mechanism for mixing substances. From a theoretical point of view, turbulence is the quintessential example of a nonlinear system far from equilibrium with many degrees of freedom. Therefore, any advancement in understanding turbulence has substantial implications and applications across multiple scientific fields.

Navier-Stokes (NS) turbulence is characterized by energy flux between different scales of motion. The direction of the net energy flux is predetermined by the dimensionality of the flow (*1*–*5*). Heuristically, in three-dimensional (3D) turbulence, energy injected at macroscopic scales generates large eddies that break down into progressively smaller ones. This energy transfer toward smaller scales, known as forward energy flux, is eventually halted by viscous dissipation (*1*, *6*). In contrast, in two-dimensional (2D) turbulence, energy is transferred from the scales where it is injected to larger scales—a process known as inverse energy flux. This energy is then either dissipated or accumulated at the largest available scale (Fig. 1A) (*7*–*9*).

Here, we study an intriguing yet pragmatic question of whether the direction of net turbulent energy flux can be manipulated by a suitable forcing scheme. Our manipulation approach is based on a simple observation that the turbulent cascade process can be recast into a mechanical process (*10*) where stress (analogous to force) and the rate of strain (analogous to displacement) at different scales of motion can work with or against each other to generate positive or negative work between scales. In 2D turbulence, both stress and the rate of strain are represented as second-order tensors. When the stress tensor aligns with the rate of strain tensor, small scales do work on larger scales, resulting in an inverse energy flux. Conversely, forward energy flux emerges when these two tensors are perpendicular (Fig. 1). This mechanical picture immediately underscores the critical role of geometry in determining the direction of spectral energy flux. The key to manipulating energy flux lies in controlling the alignment between these two tensors. If this intuitive framework holds, it could enable the generation of unconventional types of NS turbulence—specifically, 3D turbulence with a net inverse energy flux and 2D turbulence with a net forward energy flux. Here, we focus on manipulating the 2D flow and show the successful control of net energy flux direction through both electromagnetically driven thin-layer flow experiments and direct numerical simulations. The framework can be extended to 3D flows as well.

RESULTS

Theoretical framework of tensor alignment

Filtering is an archetypal method for examining interactions between different scales in a nonlinear system. By applying a filter to a nonlinear equation at a given length scale, the nonlinearity produces new terms in the filtered equation that capture the interaction between the degrees of freedom that are retained and those that are removed. In other words, these new terms act as source or sink terms for the remaining degrees of freedom. For example, applying a low-pass filter, i.e., removing scales of motion that are smaller than a certain cutoff length scale (L), to the NS equations introduces the subgrid-scale stress $\tau_{ij}^{(L)} = \left(u_i u_j\right)^{(L)} - u_i^{(L)} u_j^{(L)}$ into the filtered NS equations, where u_i is the ith component of the fluctuating velocity. This stress term depicts the momentum transfer across the length scale L. Similarly, inspecting the equation of motion for filtered kinetic energy ($E^{(L)} = \frac{1}{2} u_i^{(L)} u_i^{(L)}$) yields a spectral energy flux term $\Pi^{(L)} = -\tau_{ij}^{(L)} s_{ij}^{(L)}$, representing the energy flux between unresolved and resolved scales, where $s_{ij}^{(L)} = (1/2)\left(\partial u_i^{(L)} / \partial x_j + \partial u_j^{(L)} / \partial x_i\right)$ is the filtered rate of strain (see Materials and Methods). Recalling the analogy introduced earlier, $\tau_{ij}^{(L)}$ is analogous to force and $s_{ij}^{(L)}$ is analogous to displacement. The inner product between these terms determines the work done from filtered (smaller) scales to retained (larger) scales through length scale L, which represents the spectral energy flux between scales of motion. Manipulating $\Pi^{(L)}$ is the primary goal of this study.

This interpretation highlights the critical importance of geometric alignment between the two tensors $\tau_{ij}^{(L)}$ and $s_{ij}^{(L)}$ (Fig. 1). When $\tau_{ij}^{(L)}$ and $s_{ij}^{(L)}$ are aligned, $\Pi^{(L)} < 0$, indicating inverse energy flux toward

[1]Department of Civil and Environmental Engineering, University of Pittsburgh, Pittsburgh, PA 15261, USA. [2]Dipartimento di Fisica Generale and INFN, Universitá di Torino, Torino, 10125, Italy. [3]Department of Mechanical Engineering and Materials Science, University of Pittsburgh, Pittsburgh, PA 15261, USA.
*Corresponding author. Email: lei.fang@pitt.edu

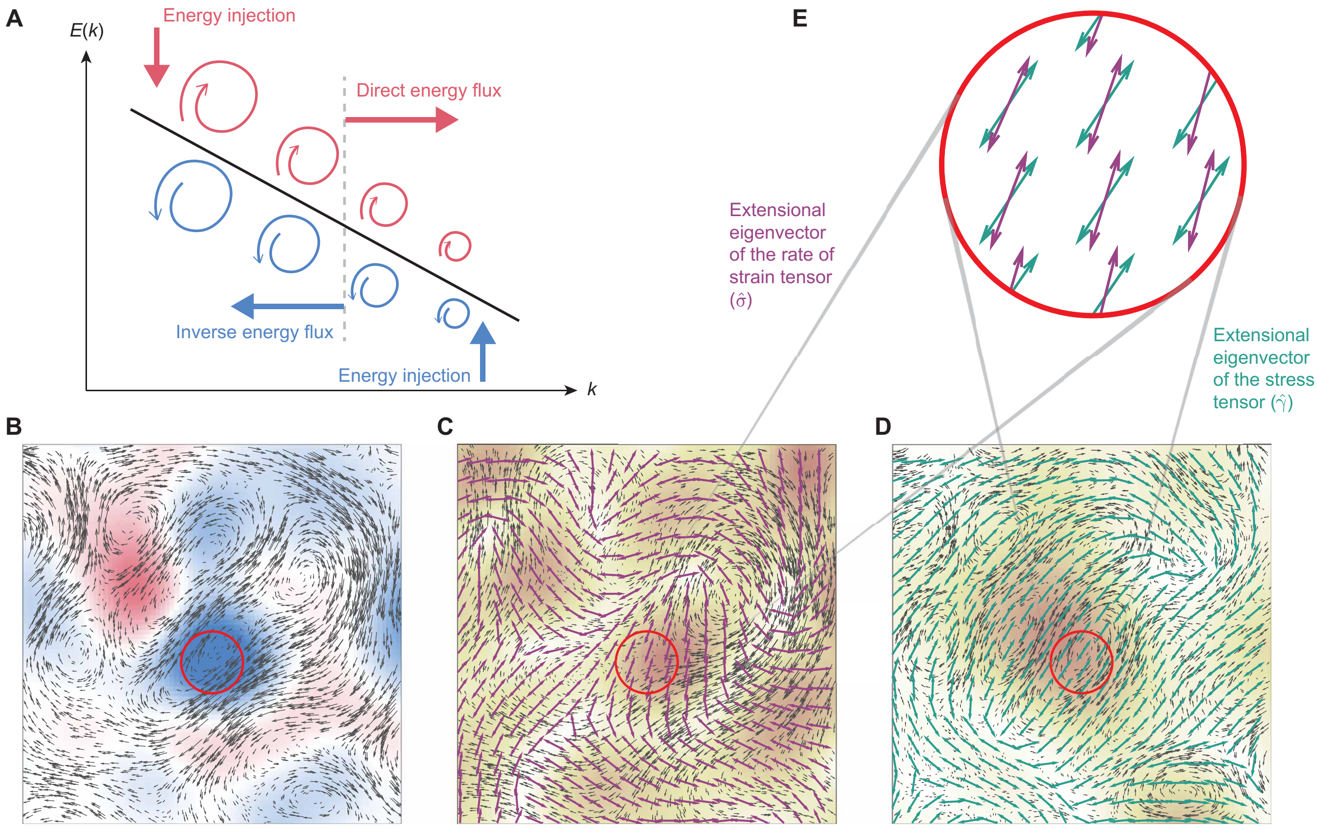

Fig. 1. Spectral energy flux and tensor geometry. (**A**) Schematic representation of spectral energy flux in turbulence. For forward energy flux (red), energy injected at large scales cascades to progressively smaller scales until it is dissipated by viscous forces. For inverse energy flux (blue), energy is injected at small scales and then transferred to progressively larger scales. This energy is either dissipated or piles up at the largest scale available within the system, defined by the system's size. These processes are quantitatively described by the energy spectrum $E(k)$, which denotes the distribution of kinetic energy across modes with wave number $k = 2\pi / L$. (**B**) Instantaneous velocity field (gray arrows) overlaid on a spectral energy flux map for 2D weakly turbulent flow. Consistent with the color scheme in (A), the red color represents forward energy flux, and blue stands for inverse energy flux. The intensity of the color indicates the magnitude. (**C**) Large-scale velocity $u_i^{(L)}$ (gray arrows) for the same 2D turbulent flow, with $L / W = 0.8$, where W is half of the domain size. Purple double-headed arrows indicate the local direction of $\hat{\sigma}$, and the background color shows the magnitude of σ. (**D**) Small-scale velocity $u_i - u_i^{(L)}$ (gray arrows) for the same 2D turbulent flow. Green double-headed arrows indicate the local direction of $\hat{\gamma}$, and the background color shows the magnitude of γ. (**E**) Zoomed-in view of tensor geometry, showing the alignment between the extensional eigenvectors of the rate of strain tensor (purple) and of the stress tensor (green). The local spectral energy flux depends on the tensor geometry, as described by Eq. 1. The alignment between these two eigenvectors in the circled region is consistent with the energy flux direction in (B).

larger length scales. Conversely, when $\tau_{ij}^{(L)}$ and $s_{ij}^{(L)}$ are perpendicular, $\Pi^{(L)} > 0$, indicating forward energy flux toward smaller length scales (Fig. 1). Furthermore, $\Pi^{(L)}$ can be reexpressed as a function that depends on the geometric alignment between the eigenframes of $\tau_{ij}^{(L)}$ and $s_{ij}^{(L)}$. In the 2D flow, this relationship is described by the following equation (*10*, *11*)

$$\Pi^{(L)} = -2\gamma\sigma\cos\left(2\theta^{(L)}\right) \quad (1)$$

where σ and γ are the largest eigenvalues of the rate of strain and the deviatoric part of stress tensors, respectively, and $\theta^{(L)}$ is the angle between the corresponding (extensional) eigenvectors $\hat{\sigma}$ and $\hat{\gamma}$. It is then clear that the alignment of the stress and the rate of strain tensor can determine not only the magnitude but also the direction of the energy flux. When $\theta^{(L)} < \pi / 4$, energy fluxes to larger scales, generating inverse energy flux; when $\theta^{(L)} > \pi / 4$, energy fluxes to smaller scales, resulting in forward energy flux. No net energy flux occurs when $\theta^{(L)} = \pi / 4$. In typical isotropic 2D turbulent flows, the alignment between stress and the rate of strain tensor is self-organized, leading to a net inverse energy flux. Previous researchers have proposed treating $\eta = \cos\left(2\theta^{(L)}\right)$ as a measure of the efficiency of energy flux between scales (*10*). The rationale behind this definition is that η represents the ratio between the observed energy flux and the maximum geometrically achievable flux, as determined by tensor geometry. It was found that the efficiency in typical isotropic 2D turbulent flow is relatively low, with an η of only 27%, as reported in previous experiments (*10*), indicating that a large portion of the geometrically possible energy flux is not realized.

In principle, by generating a background flow with an ordered rate of strain and perturbing it with directionally biased stresses, we can control the tensor geometry between stress and the rate of strain tensors, thereby manipulating the efficiency of the net energy flux based on Eq. 1. In this study, we selected hydrodynamic shear as the background flow, establishing a well-organized large-scale rate of strain orientation (Fig. 2B), and perturbed it with a directionally biased monopole-like perturbation (Fig. 2C). The direction of $\hat{\gamma}$ from

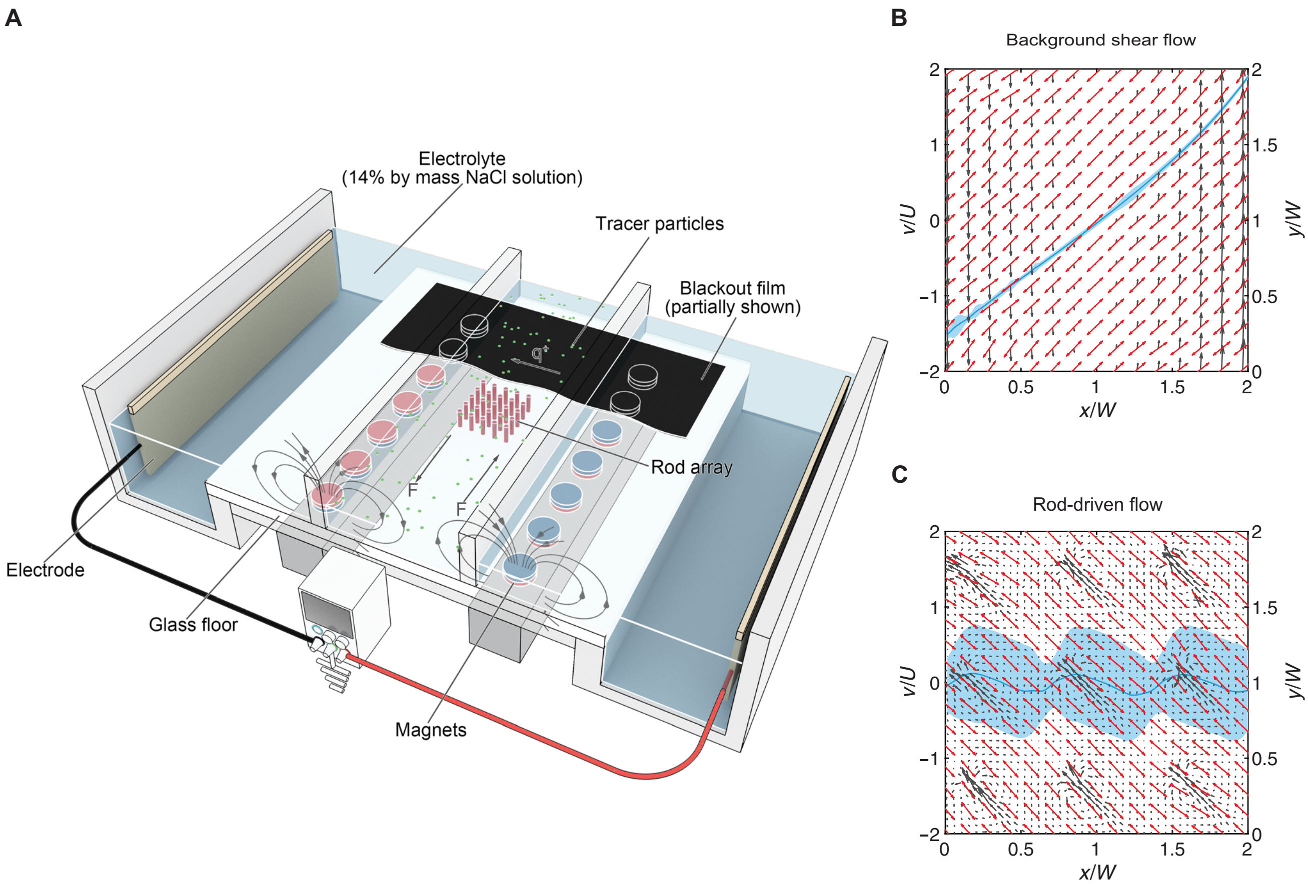

Fig. 2. Experimental setup and characterization of the background flow and physical perturbations. (**A**) Schematic of the experimental setup. The cross section of the experimental setup illustrates the thin fluid layer and tracer particles at the surface (not to scale). A pair of electrodes conducts direct current horizontally through the electrolyte. The vertical magnetic field from the permanent magnets interacts with the horizontal direct current to generate the Lorentz force on the fluid, which acts nearly within the plane. The tracer particle on the fluid's surface represents the 2D space under study. A rod array is controlled by a linear actuator, which can introduce directionally biased physical perturbations. (**B**) Flow field of the hydrodynamic shear (gray arrows). Red double-headed arrows indicate the extensional direction of $s_{ij}^{(L)}(\hat{\sigma})$. (**C**) Flow field of a moving rod array in quiescent fluid (gray arrows). Red double-headed arrows indicate the extensional direction of $\tau_{ij}^{(L)}(\hat{\gamma})$. The blue curves in (B) and (C) represent the assembled average of the *v* component of velocity along the *x* axis, normalized by the root-mean-square velocity *U*. Shaded areas indicate the standard deviation of the *v* component of velocity normalized by *U*. The assembled average was calculated both temporally and spatially along the *y* axis. Arrows in the velocity and eigenvector fields were downsampled for clearer visualization.

the monopole-like perturbation is found to align with the direction of the applied monopole forces (see Materials and Methods). Consequently, by controlling the mechanical angle θ between the direction of $\hat{\sigma}$, associated with the background shear flow, and the direction of the monopole forces, we can substantially manipulate the direction of the spectral energy flux.

Experiments and numerical simulation of energy flux manipulation

To apply this theoretical framework for manipulating energy flux, we conducted experiments using an electromagnetically driven thin-layer flow system (Fig. 2A) (*8*, *12*, *13*). We generated a steady shear flow to establish a well-ordered large-scale rate of strain via the Lorentz body force that arose from the interaction between the magnetic field produced by two stripes of magnets with opposite polarities and a direct current passing through the electrolyte layer (Fig. 2B). The physical perturbation was introduced using a 5 by 5 grid of rods driven by a programmable linear actuator at a velocity of 1 cm/s in a forward-and-back manner (Fig. 2C). The flow was then recorded and analyzed using a particle tracking velocimetry algorithm (see Materials and Methods) (*14*).

The numerical simulations were performed using a standard fully dealiased pseudospectral code (*15*, *16*). NS equations were integrated on a 2D domain with a second-order Runge-Kutta temporal scheme. The linear hydrodynamic shear was generated by simulating a Couette flow between two walls. Local physical perturbation was applied via a 5 by 5 array of force monopoles. The strength of monopoles had a pulsating force varying sinusoidally (see Materials and Methods).

Manipulated net spectral energy flux

We summarize our experimental and simulation results of energy flux manipulation in Fig. 3 (*17*), where a considerable correlation between the controlled mechanical angle (θ) and the measured tensor alignment angle ($\theta^{(L)}$) was observed. In our experiments, we conducted three control cases. The first involved pure shear flow

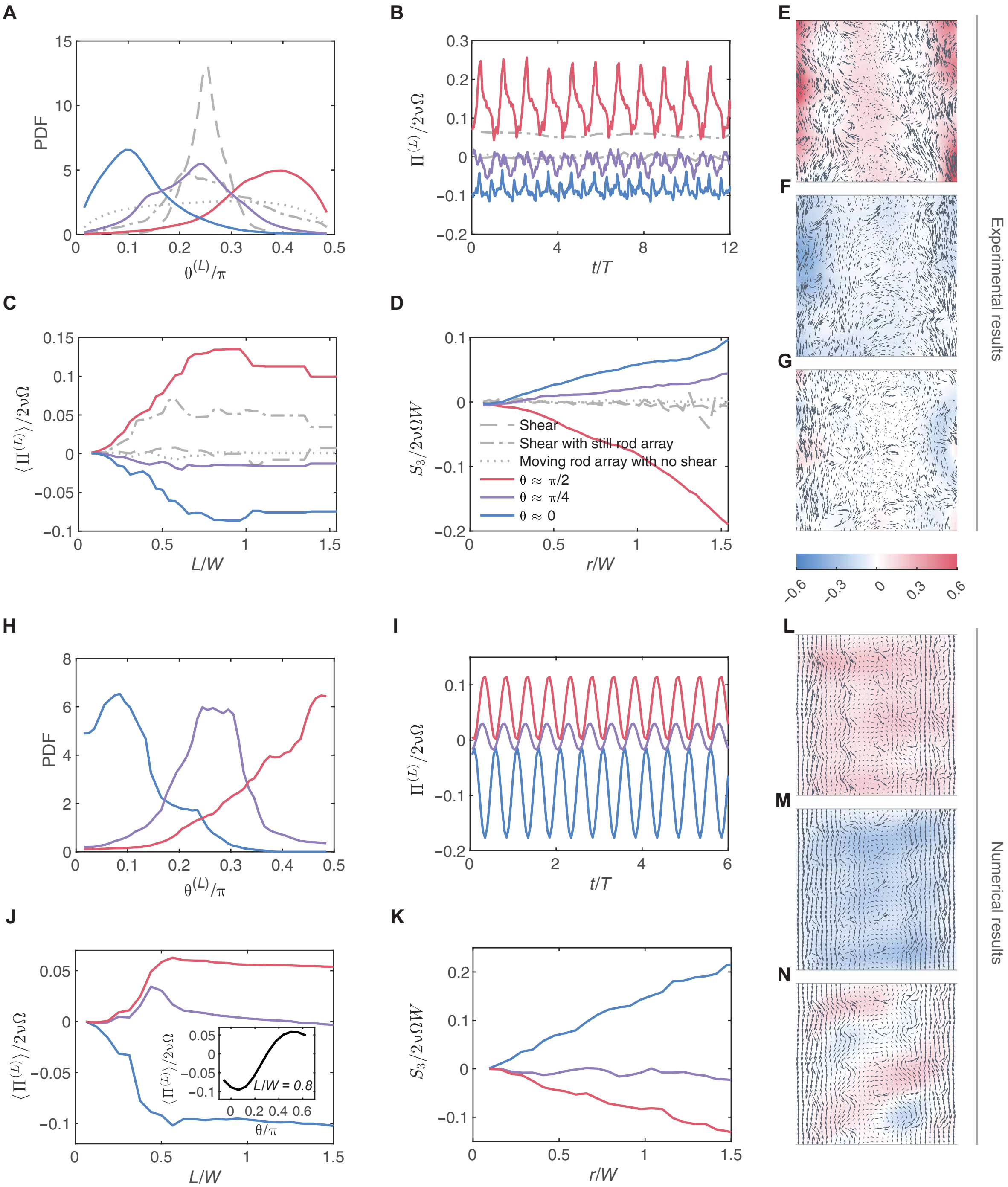

Fig. 3. Experimental and numerical results of energy flux manipulation. This figure illustrates how the mechanical angle, θ, affects tensor alignment, subsequently influencing energy flux in both experimental and simulation results. (**A** and **H**) Probability density functions (PDFs) of tensor alignment angle ($\theta^{(L)}$) with $L / W = 0.8$ for both experiments and simulations, where W is half of the domain size for experiments and simulations, showing that different forcing conditions produce distinct tensor alignment distributions. (**B** and **I**) Temporal evolution of spatially averaged $\Pi^{(L)}$ with $L / W = 0.8$ for experiments and simulations, respectively. (**C** and **J**) $\Pi^{(L)}$ at different L values for experiments and simulations, respectively. The inset of (J) is the $\Pi^{(L)}$ at $L / W = 0.8$ for a range of mechanical angle (θ). (**D** and **K**) Third-order structure function S_3 at different displacement r for experiments and simulations, respectively. (**E** to **G** and **L** to **N**) Snapshots of spatial distribution of energy flux for $\theta \approx \pi / 2$, $\theta \approx \pi / 4$, and $\theta \approx 0$, respectively. (E) to (G) correspond to experiments and (L) to (N) correspond to simulations. The gray arrows are flow velocity vectors, and the color maps show the magnitude of spectral energy flux $\Pi^{(L)}$ All times are normalized by T, which represents the rod array's moving period for experimental results and the blinking period of the monopole array for simulation results. All lengths are normalized by half the domain size. $\Pi^{(L)}$ is normalized by viscous dissipation $2\nu\Omega$, where Ω is the spatially averaged vorticity square. Overall, these panels collectively demonstrate that the direction and magnitude of turbulent energy flux can be systematically manipulated via tensor alignment, and this manipulation is observed consistently across experimental and numerical systems.

without perturbation. In the second case, we introduced a static rod array into the shear flow, ensuring that any changes in tensor geometry were not due to the rod array acting as a new boundary condition. The third control case was the rod array moving in a quiescent fluid to rule out the possibility that the energy flux manipulation was due to the rod array moving alone. As shown in Fig. 3A, in all three control cases, $\theta^{(L)}$ was symmetrically distributed around $\pi/4$, resulting in an efficiency η close to zero. Consequently, we observed only a relatively weak spectral energy flux in these control cases (Fig. 3C).

When we aligned the added stress with the background rate of strain ($\theta \approx 0$), we observed a salient shift of $\theta^{(L)}$ toward 0 (Fig. 1A). Similarly, we observed a substantial shift toward $\theta^{(L)} = \pi/2$ as we applied the added stress perpendicularly with the background rate of strain ($\theta \approx \pi/2$). As our manipulation set θ to approximately $\pi/4$, $\theta^{(L)}$ was symmetrically distributed around $\pi/4$, resulting in only a small net energy flux between scales (Fig. 3, A and H). The direct numerical simulations allowed for fine-tuning the direction of the monopole array. In the inset of Fig. 3J, we present the energy flux as a function of different mechanical angles θ. We see that the energy flux varied with θ in a sinusoidal manner that reflected the form of Eq. 1. Theoretically, the maximum inverse energy flux should occur when $\theta^{(L)} = 0$, and the maximum forward energy flux will emerge when $\theta^{(L)} = \pi/2$. In our observations, the maximum inverse and maximum forward angle alignments occurred at $\theta = \pi/16$ and $\theta = \pi/2$, respectively. The slight discrepancy between the optimal θ and optimal $\theta^{(L)}$ for maximum inverse energy flux is likely due to the engineered tensor alignment being slightly altered during the coupling, an inherent nonlinear process, between the physical perturbation and the background flow.

We calculated the energy flux between scales based on the measured stress and the rate of strain tensors. In Fig. 3 (B and I), we present the time series of the spatially averaged energy flux. Although the time series of energy flux correlated with the forward-and-back motion of the rod array in experiments and with the blinking of the monopoles in simulations, the energy flux directions remained consistent with the manipulated geometric alignments. We also calculated the net energy flux across different cutoff scales (Fig. 3, C and J). Consistent with the tensor geometry statistics, the motion of the rod and monopole arrays considerably influenced the direction of the energy flux by introducing directionally biased small-scale stresses.

A further observable related to the direction of energy transfer is the third-order longitudinal structure function $S_3(r) = \left\langle \left[\Delta_r \mathbf{u} \cdot \hat{\mathbf{e}}_\mathbf{l}\right]^3 \right\rangle$, where $\hat{\mathbf{e}}_\mathbf{l}$ is the unit vector in the longitudinal direction and $\Delta_r \mathbf{u} = \mathbf{u}\left(\mathbf{x} + r\hat{\mathbf{e}}_\mathbf{l}\right) - \mathbf{u}(\mathbf{x})$ is the velocity difference over displacement r. While the filtering approach in Eq. 1 accesses different scales by spatial filtering, $S_3(r)$ encodes the information on the dynamics at each scale via the statistics of the velocity difference at the corresponding displacements in the physical space. As shown in Fig. 3 (D and K), the third-order structure function changes sign with θ. This can be interpreted in view of well-known results valid for the inertial range of large-Reynolds-number turbulent flows. In that case, one can show that $S_3 = -C\epsilon r$, where ϵ is the (positive) energy dissipation rate, while C is a constant whose sign depends on the direction of the cascade. In 3D flows (where the flux is positive), $C = \frac{4}{5}$ (*18*), while $C = -\frac{3}{2}$ (*19*) in the 2D flow, where the energy flux is negative and an inverse, upscale energy cascade is observed. Although, at our relatively low Reynolds numbers, the scaling results do not apply, one can expect $S_3 < 0$ for a direct energy flux and $S_3 > 0$ for an inverse one, which is consistent with the observation. Therefore, the sign of S_3 provides an additional signature of the direction of spectral energy flux, complementing the filtering results. We emphasize that $S_3(r)$ is used here only as a qualitative cross-check rather than an independent proof of energy flux direction. It has been highlighted that caution is needed when interpreting $S_3(r)$ in 2D turbulence because the $S_3(r)$ law varies with different flow conditions and nonideal effects, such as large-scale drag, can considerably affect the sign of $S_3(r)$ (*20*).

Notably, we have both experimentally and numerically produced 2D weak turbulence with net forward energy flux, a phenomenon contrary to classical expectations (Fig. 3, E and L). This is particularly noteworthy because traditional 2D turbulence, as predicted by Kraichnan (*3*), exhibits a net inverse energy flux. The creation of this atypical type of turbulence provides a unique opportunity to compare it with its traditional counterpart, potentially deepening our understanding of the turbulent cascade process. Specifically, by providing a mechanical perspective on spectral energy transfer, our findings suggest a framework for probing the longstanding question of why, statistically, naturally occurring 2D turbulent flows tend to maintain a net inverse energy flux—or, in the language of tensor geometry, why they favor an average alignment angle below $\pi/4$ (*21*, *22*). From an application perspective, reversing the natural direction of energy flux may induce profound kinematic and dynamical differences that may not only enhance our understanding of natural processes but also improve our ability to control engineered systems.

DISCUSSION

Our analysis demonstrates that directionally biased physical perturbation can couple with the background flow, causing distinct yet predictable directions of spectral energy flux. Directionally biased physical perturbations are prevalent in both natural and engineered systems. Therefore, our results have broad applications and implications in both natural and engineered systems, spanning length scales from millimeters in microfluidic mixers to hundreds of kilometers in geophysical flows (Fig. 4).

On the millimeter scale, microfluidic mixers often suffer from poor mixing (*23*, *24*). Our findings offer valuable insights into addressing this issue. By engineering the flow in microfluidic mixers at a low Reynolds number to induce forward energy flux, it is possible to generate smaller scales of motion, thereby enhancing mixing efficiency.

Biologically generated ocean mixing plays a crucial role in understanding the biogeochemical structure of the water column in climatically important regions of the ocean (*25*–*27*). Contrary to traditional belief, a recent study has shown that a swimmer's ability to mix the local flow is not an immutable trait but varies depending on the swimmer's alignment relative to local shear. The study demonstrated that flows generated by a group of swimmers can couple with background flows to enhance mixing (*12*). Moreover, the interaction between the directionally biased stress from a swimmer and a background hydrodynamic shear can induce appreciable differences in spectral energy transfer properties and modify the strength of background hydrodynamic shear (*13*). Therefore, the coupling

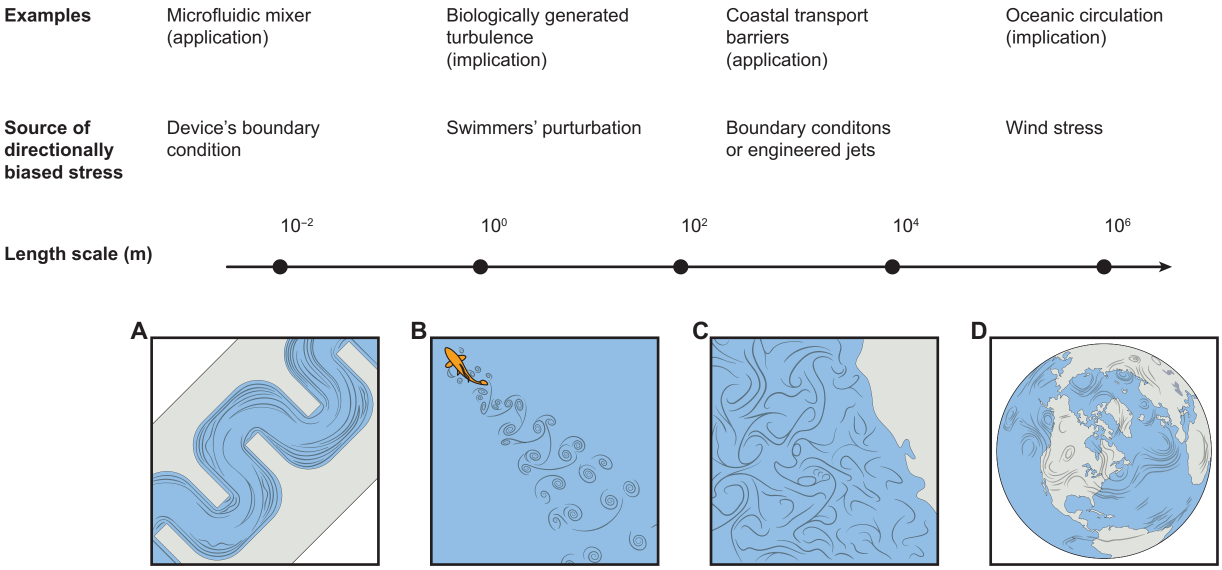

Fig. 4. Applications and implications in natural and engineered systems. Spectral energy flux manipulation can occur in systems spanning scales from 10^{-3} to 10^{6} m. This manipulation occurs either through engineering (A and C) or via natural processes (B and D). (**A**) By engineering appropriate boundary conditions that interact with fluid to generate directionally biased stress, we can force forward energy flux even at a Reynolds number of order 1, as our theoretical framework remains valid. The increase in small-scale energy will generate fine-scale eddies that facilitate mixing in microfluidic mixers. (**B**) In nature, biologically generated agitation is found to be able to couple with the background hydrodynamic shear to generate either forward or inverse energy flux. This process can either attenuate or strengthen the background hydrodynamic shear, affecting the local biogeochemical structure of the water column. (**C**) Engineered boundary conditions or directionally biased jets with moderate energy can considerably affect LCSs in coastal oceans. In Materials and Methods, we present a theoretical estimation of the energy power needed to actively manipulate LCSs. (**D**) Climate change will profoundly alter wind fields and oceanic flows. Our results suggest that the altered wind stress could profoundly affect the direction of energy flux in the oceanic flow because of varying alignments between wind stress and oceanic flow.

between directionally biased stress from swimmers and background flow is of great importance in understanding the impact of biologically generated turbulence on ocean mixing.

In coastal oceans, Lagrangian Coherent Structures (LCSs), which can span several kilometers, act as transport barriers in geophysical flows, hindering effective mixing in coastal areas and potentially contributing to the formation of ocean forbidden zones (*28*, *29*). Disrupting these LCSs in coastal regions could alleviate these forbidden zones and improve the health of coastal ecosystems. Our theoretical framework offers a method to engineer optimal small-scale stress that couples with the background flow to enhance forward energy flux. The enhanced forward energy flux will dump energy that sustains the large-scale LCSs to smaller scales, where, eventually, it can be dissipated by viscosity. In the Supplementary Materials, we present a theoretical estimation demonstrating the feasibility of manipulating LCSs. This estimation suggests that it is possible to substantially influence LCSs using only 0.05% of the energy that sustains them.

In geophysical systems, wind stresses consistently do positive or negative work to facilitate energy exchange between atmospheric and oceanic systems (*30*–*32*). Beyond this traditional first-order view of energy exchange, our results indicate that a profound second-order effect may arise when local wind stresses act as biased stresses. These biased wind stresses could interact with the rate of strain of the oceanic flow, leading to distinct directions of energy flux among different scales of motion in oceanic flows. While this remains a hypothetical extension and has not yet been tested, this hypothesis provides valuable insights and offers a promising framework for understanding the multiscale dynamics of geophysical flows. In the context of climate change, alterations in the flow patterns of either atmospheric or oceanic systems can influence not only the energy exchange between these systems but also the direction of energy flux within the oceanic flow system, potentially reshaping large-scale circulation and transport dynamics.

To conclude, we have developed a theoretical framework for manipulating the direction of spectral energy flux through tensor geometry. This theoretical framework was demonstrated through the successful manipulation of spectral energy flux of the 2D flow in both experiments and simulations. Beyond its theoretical significance, our framework has profound applications and implications for natural and engineered systems ranging from microfluidic mixers and biologically generated turbulence to geophysical flows.

MATERIALS AND METHODS

Filtering approach and spectral energy flux term

Filter space technique

The filter space technique is based on a filtering process (*33*) and can extract spatially localized scale-to-scale energy flux information from measured flow fields (*34*). The filtering process can be generally expressed as a convolutional integral (*35*). For example, the filtered component of a velocity field has the form

$$u_i^{(\mathrm{L})}(\mathbf{x}) \equiv \int G^{(L)}(\mathbf{r},\mathbf{x})u_i(\mathbf{x}-\mathbf{r})d\mathbf{r} \tag{2}$$

where $G^{(L)}$ is a kernel acting as a low-pass filter, with the superscript L indicating the cutoff length scale. Our result is not sensitive to the specific nature of the filter kernel. Here, we used a sharp spectral filter (with a cutoff length L) smoothed by a Gaussian window to avoid the ringing effect.

To obtain the spectral energy flux term $\Pi^{(L)}$, we start from filtering the NS equations that govern the motion for incompressible fluids

$$\frac{\partial u_i}{\partial t}+u_j\frac{\partial u_i}{\partial x_j}=-\frac{1}{\rho}\frac{\partial p}{\partial x_i}+\nu\frac{\partial^2 u_i}{\partial x_j\partial x_j} \text{ and } \frac{\partial u_i}{\partial x_i}=0 \tag{3}$$

in which u_i is the ith component of velocity, ρ is the density, p is the pressure, and ν is the kinematic viscosity. After applying the filter, we can obtain the evolution equation for the filtered velocity field $u_i^{(L)}$ as

$$\frac{\partial u_i^{(L)}}{\partial t}+u_j^{(L)}\frac{\partial u_i^{(L)}}{\partial x_j}=-\frac{1}{\rho}\frac{\partial p^{(L)}}{\partial x_i}+\nu\frac{\partial^2 u_i^{(L)}}{\partial x_j\partial x_j}-\frac{\partial \tau_{ij}^{(L)}}{\partial x_j} \tag{4}$$

where $\tau_{ij}^{(L)}=\left(u_iu_j\right)^{(L)}-u_i^{(L)}u_j^{(L)}$.

Taking the inner product of $u_i^{(L)}$ and the filtered momentum Eq. 4, we can obtain the equation of motion for the filtered kinetic energy $E^{(L)}=\frac{1}{2}u_i^{(L)}u_i^{(L)}$ as

$$\frac{\partial E^{(L)}}{\partial t}=-\frac{\partial J_i^{(L)}}{\partial x_i}-\nu\frac{\partial u_i^{(L)}}{\partial x_j}\frac{\partial u_j^{(L)}}{\partial x_i}-\Pi^{(L)} \tag{5}$$

where $\Pi^{(L)}=-\tau_{ij}^{(L)}s_{ij}^{(L)}$ with $s_{ij}^{(L)}=\frac{1}{2}\left(\partial u_i^{(L)}/\partial x_j+\partial u_j^{(L)}/\partial x_i\right)$ being the rate of strain tensor for the filtered velocity field. On the right-hand side of Eq. 5, the term with $J_i^{(L)}$ assembles all the terms that represent the spatial currents of filtered energy. The second term represents the viscous damping of energy within the resolved scales. The term $\Pi^{(L)}$, in particular, represents the spectral energy flux between scales smaller than L and scales larger than L. $\Pi^{(L)}<0$ indicates inverse energy flux toward larger length scales. $\Pi^{(L)}>0$ indicates forward energy flux toward smaller length scales.

Spectral energy flux term decomposition

The stress tensor $\tau_{ij}^{(L)}$ can be further decomposed into three components (*4*, *35*, *36*) on the basis of the type of triad interaction as

$$\begin{aligned}\tau_{ij}^{(L)}=&\left(u_i^{(L)}u_j^{(L)}\right)^{(L)}-u_i^{(L)}u_j^{(L)}\\&+\left[u_i^{(L)}\left(u_j-u_j^{(L)}\right)\right]^{(L)}+\left[u_j^{(L)}\left(u_i-u_i^{(L)}\right)\right]^{(L)}\\&+\left[\left(u_i-u_i^{(L)}\right)\left(u_j-u_j^{(L)}\right)\right]^{(L)}\end{aligned} \tag{6}$$

The first component $\tau_L^{(L)}=\left(u_i^{(L)}u_j^{(L)}\right)^{(L)}-u_i^{(L)}u_j^{(L)}$ is a small-scale quantity composed of two large-scale quantities. The second component $\tau_C^{(L)}=\left[u_i^{(L)}\left(u_j-u_j^{(L)}\right)\right]^{(L)}+\left[u_j^{(L)}\left(u_i-u_i^{(L)}\right)\right]^{(L)}$ is a large-scale quantity composed of one large-scale quantity and one small-scale quantity. The third component $\tau_S^{(L)}=\left[\left(u_i-u_i^{(L)}\right)\left(u_j-u_j^{(L)}\right)\right]^{(L)}$ is a large-scale quantity composed of two small-scale quantities. In large eddy simulation, the three terms are called Leonard stress, cross stress, and subgrid-scale Reynolds stress, respectively. We take these names here for convenience. However, note that u_i here contains information about all scales of motion and, hence, the term $\tau_{ij}^{(L)}$ involves no modeling, which is different from large eddy simulation. The inner products of these components with $s_{ij}^{(L)}$ give the corresponding components of the spectral energy flux $\Pi^{(L)}$ as $\Pi_L^{(L)}$, $\Pi_C^{(L)}$, and $\Pi_S^{(L)}$

$$\Pi^{(L)}=\Pi_L^{(L)}+\Pi_C^{(L)}+\Pi_S^{(L)} \tag{7}$$

$$\Pi_L^{(L)}=-\tau_L^{(L)}s_{ij}^{(L)} \tag{8}$$

$$\Pi_C^{(L)}=-\tau_C^{(L)}s_{ij}^{(L)} \tag{9}$$

$$\Pi_S^{(L)}=-\tau_S^{(L)}s_{ij}^{(L)} \tag{10}$$

In (*36*), it has been shown that the subgrid term $\Pi_S^{(L)}$ carries most of the net spectral energy flux information between the large and small scales. The Leonard term and the cross term involve more subtle interpretations. Using a simple cellular flow, Liao and Ouellette (*36*) showed that the Leonard term is dominated by the transfer of energy between different resolved wave vectors rather than the transfer of energy between large and small scales. However, after spatial averaging, they found that the Leonard term and crossing term have a negligible contribution to the net spectral energy flux, which is also verified by our experiment data of a 2D turbulent flow (see fig. S1).

Despite the theoretically negligible contribution to the spectral energy flux by the Leonard term and the cross term, including the Leonard term and the cross term will cause contamination to the calculated spatially averaged spectral energy flux, especially in regions near boundaries. Specifically, this contamination comes from edge padding when applying a filter to the measured data near boundaries. Padding involves filling artificial data (here, we used zero-padding) into the regions out of boundaries where there are no measured data so that the filtering process can be applied near boundaries. The magnitude of this padding error is small compared to the magnitude of the small-scale fluctuations ($u_i-u_i^{(L)}$) created by the moving rods. However, this padding error will be magnified when it is added to or multiplied by a large-scale velocity ($u_i^{(L)}$). Therefore, here, we used the subgrid flux term $\Pi_S^{(L)}$ in our analysis instead of $\Pi^{(L)}$. For simplicity and clarity, we omitted the subscript in both the figures and the main text.

Theoretical background for tensor geometry

Rewriting the spectral energy flux term

The theory of tensor geometry is described in detail in (*10*, *37*). Here, we just briefly introduce the necessary information. Because the rate of strain tensor $s_{ij}^{(L)}$ is symmetric and deviatoric, we can just consider the deviatoric part of the stress tensor when calculating the spectral energy flux because only this part will affect the inner product (*38*). Both the rate of strain tensor and deviatoric part of the stress tensor have two eigenvalues with the same magnitude and opposite sign. The eigenvector corresponding to the positive eigenvalue (referred to as extensional) and the eigenvector corresponding to the negative eigenvalue (referred to as compressional) are orthogonal. We label the extensional eigenvalue for the stress tensor as γ and that for the rate of strain tensor as σ. Working in the eigenbasis of the stress tensor and marking the angle between the extensional eigenvectors of these two tensors as $\theta^{(L)}$, we have

$$\begin{aligned} -\Pi^{(L)} &= \tau_{ij}^{(L)} s_{ij}^{(L)} \\ &= Tr\left[\begin{pmatrix}\gamma & 0\\ 0 & \gamma\end{pmatrix}\begin{pmatrix}\cos(\theta^{(L)}) & -\sin(\theta^{(L)})\\ \sin(\theta^{(L)}) & \cos(\theta^{(L)})\end{pmatrix}\begin{pmatrix}\sigma & 0\\ 0 & \sigma\end{pmatrix}\begin{pmatrix}\cos(\theta^{(L)}) & \sin(\theta^{(L)})\\ -\sin(\theta^{(L)}) & \cos(\theta^{(L)})\end{pmatrix}\right] \\ &= 2\gamma\sigma\cos(2\theta^{(L)}) \end{aligned} \quad (11)$$

Note that using $\tau_{ij}^{(L)}$ or $\tau_S^{(L)}$ does not affect the derivation of Eq. 11. Because both γ and σ are positive, we can see that the direction of spectral energy flux depends only on the alignment of the eigenframes of the two tensors.

Tensor geometry of the large-scale shear

Through the perspective of tensor geometry, there arises the possibility of manipulating the spectral energy flux by forcing the small-scale stress to align with the large-scale rate of strain in any intended angle. To demonstrate this, first consider a cutoff length scale L. At large scales, there exists a steady shear flow whose width is much larger than L. To simplify this problem, we set the steady shear flow with streamlines aligning with the y axis and with no stream-wise velocity gradient. In the x direction, the shear has a constant velocity gradient K for the vertical velocity component. The rate of strain tensor of the shear flow at any length scale L is then

$$s_{ij}^{(L)} = \begin{bmatrix} 0 & \frac{1}{2}K \\ \frac{1}{2}K & 0 \end{bmatrix} \quad (12)$$

Because this matrix is traceless and symmetric, it has two eigenvalues of the same magnitude but with opposite signs. The two eigenvectors are orthogonal, and the angle between the extensional eigenvector and the x axis has an angle of $\pi/4$ (or $5\pi/4$). If we apply disturbances to the large-scale shear flow with injection length scales much smaller than L, the nonlinear coupling between the applied small-scale stresses and the background flow will result in turbulent flow that transfers energy through scales.

Tensor geometry of the small-scale stresses

Here, we demonstrate how we generate engineered small-scale stress through physical perturbations. For simplicity, consider the small-scale disturbance as a velocity vector b_i that forms an angle θ_b with the x axis. Given enough scale separation between the small-scale disturbance and the large-scale shear, we would expect that most of the information induced by the small-scale disturbance will be included in the residue after filtering. Therefore, we can estimate that $b_i \approx u_i - u_i^{(L)}$. The deviatoric part of the subgrid-scale Reynolds stress is thus

$$\begin{aligned} \tau_S^{(L)} &= \left(b_i b_j\right)^{(L)} \\ &= \left(\|b_i\|^2 \begin{bmatrix} \cos^2(\theta_b) - \frac{1}{2} & \sin(\theta_b) * \cos(\theta_b) \\ \sin(\theta_b) * \cos(\theta_b) & \sin^2(\theta_b) - \frac{1}{2} \end{bmatrix}\right)^{(L)} \end{aligned} \quad (13)$$

We note that the filtering process will not affect the eigenvector direction. We can get that the extensional eigenvector for the deviatoric subgrid-scale Reynolds stress $\tau_S^{(L)}$ is in the direction of $\begin{pmatrix} 1 \\ \tan(\theta_b) \end{pmatrix}$. Therefore, the direction of the extensional eigenvector of $\tau_S^{(L)}$ is in parallel with the direction of b_i.

From the derivations above, we can see that the directions of the extensional eigenvectors for both $s_{ij}^{(L)}$ and $\tau_S^{(L)}$ are known even before applying physical perturbations to the background flows. Therefore, on the basis of Eq. 11, it is possible to manipulate the direction of spectral energy flux by controlling the alignment between the eigenframes of these two tensors.

Quasi-2D turbulence experiments

Apparatus and particle tracking

The main body for the quasi-2D flow system consisted of an acrylic frame, a pair of copper electrodes installed on the opposite sides of the setup, and a piece of tempered glass in the center separating a thin layer of salt water on top and an array of cylindrical magnets below. The dimensions of the main frame and the glass floor in the center were 96.5 cm by 83.8 cm and 81.3 cm by 81.3 cm, respectively. We coated the upper surface of the glass with hydrophobic materials (Rain-X) to reduce friction and covered the lower surface by a light-absorbing blackout film. Beneath the glass, cylindrical magnets were organized in desired patterns to drive flow in different directions. Each magnet (neodymium grade N52) had an outer diameter of 1.27 cm and a thickness of 0.64 cm, with the maximum magnetic flux density of 1.5 T at the magnet surface. We loaded a thin layer (6-mm thickness) of 14% by mass NaCl solution on top of the glass. The solution had a density $\rho = 1.101\ \mathrm{g/cm^3}$ and a viscosity $\nu = 1.25 \times 10^{-2}\ \mathrm{cm^2/s}$. By passing a direct current through the conducting solution layer, we were able to drive a quasi-2D flow with the resulting Lorentz body force and control the flow Reynolds number by adjusting the direct current intensity. The 2D was well kept throughout our experiments.

To track the flow, we seeded green fluorescent polyethylene tracer particles (Cospheric) into the fluid. The tracer particles had a density of 1.025 g/cm^3 and diameters ranging from 106 to 125 μm. The Stokes number of the particles was of order 10^{-3}, which means that the particle could accurately trace the flow (*39*). Because the density of the particles was lower than that of the working fluid, they would float on the gas-liquid interface. Because of surface tension effects, they would show a slow clustering tendency, which is known as the "cheerios effect" (*40*). To reduce the surface tension, a small amount of surfactant was added to the fluid to minimize the impact on tracer movements. Our measurement of tracers in quiescent fluid showed that the "cheerios effect" was negligible.

We used a machine vision camera (Basler, acA2040-90μm) to image the flow that was illuminated by blue light-emitting diode lights. We recorded an 11.4-cm by 11.4-cm region at the center of the setup with a resolution of 1600 pixels by 1600 pixels. About 18,000 to 22,000 particles could be recorded at a frame rate of 60 frames per second. With this particle density and frame rate, we could obtain highly spatiotemporally resolved velocity fields through a particle tracking velocimetry algorithm (*14*). For easier use, we then interpolated the measured flow onto regular Eulerian grids using cubic interpolation with a grid size of 12 pixels (0.85 mm), which gave a grid density not higher than the original particle density. The final analysis to obtain Figs. 2 and 3 was performed on a 7.4-cm by 7.4-cm domain at the center of the measured area to reduce errors near boundaries caused by edge padding during filtering.

Two-dimensional steady shear flow with moving rods

We used two stripes of magnets with opposite polarity. The distance between the two stripes was 20 cm. When a direct current was conducted through the fluid, the two stripes generated a hydrodynamic shear with an ordered rate of strain (Fig. 2B). To apply the small-scale stress to couple with the rate of strain in the background flow, we built a 5 by 5 grid of rods and drove the grid with a programmable linear actuator. The diameter of each rod was 2 mm, and the center-to-center space between neighbor rods was 2.5 cm. The rod array moved back and forth at a speed of 1 cm/s to generate directionally biased stress (Fig. 2C). We define Reynolds number $Re = UW/\nu$, where U is the root-mean-square velocity, W is half of the domain width for analysis, and ν is the kinematic viscosity. The Reynolds number of the resulting flow was 210.

2D turbulence simulation

The numerical simulations were carried out using a standard fully dealiased pseudospectral code (*15*, *16*). Equation 3 was integrated on a 2D domain of size $L_x \times L_y$, with a second order Runge-Kutta temporal scheme. To simulate a configuration similar to that of the experiment we used as a base flow, a linear shear flow was obtained by imposing the boundary conditions $\mathbf{u}\left(L_x/2, y\right) = \mathbf{u}_+ = \left(0, +U_s\right)$ and $\mathbf{u}\left(-L_x/2, y\right) = \mathbf{u}_- = \left(0, -U_s\right)$ at the walls $x = \pm L_x/2$, with periodic boundary condition on the y direction. The boundary conditions were implemented via a penalization method (*41*). Specifically, at each time step, the body force

$$\mathbf{F}_{\mathrm{pen}}(\mathbf{x}) = -\lambda\left[\mathbf{u}(\mathbf{x}) - \mathbf{u}_\pm\right]\phi\left(x \mp L_x/2\right) \tag{14}$$

was imposed, with λ being a large parameter. The scalar function ϕ is a mask with support only within a small distance r_b of the boundaries and defined as $\phi(x) = \cos\left(\frac{\pi x}{2r_b}\right)$ if $|x| < r_b$ and $\phi(x) = 0$ otherwise. All the simulations presented here are performed with shear velocity $U_s = 1$ and domain sizes $L_x = 6.136$ and $L_y = 2\pi$ (arbitrary units). We used a numerical resolution of $N_x \times N_y = 500 \times 512$ grid points, which is sufficient to resolve the smallest scale in the flow, and the support of each penalization mask was $2r_b = 9.8 \times 10^{-2}$ corresponding to eight grid points.

The local forcing was applied using 25 force monopoles whose centers were organized on a regular 5 by 5 square grid with side 2.0 (approximately one-third of the span of the effective numerical channel). Each monopole applied a pulsating force $\mathbf{F}_i = f\sin(\omega t)G\left(\mathbf{x}_i\right)\mathbf{e}\left(\theta_m\right)$, where $\mathbf{x}_i$ is the position of the ith monopole, $G(\mathbf{x})$ is a two-dimensional normalized Gaussian with a half-width of four grid points, and $\mathbf{e}\left(\theta_m\right) = \left(-\sin\theta_m, \cos\theta_m\right)$ sets the direction of the force monopole at an angle θ_m with respect to the y axis. The amplitude of the monopole was $f = 0.38$.

All the numerical simulations were started from a fluid at rest $\mathbf{u} = 0$ and carried on until a shear flow $\mathbf{u} = \left(0, 2xU_s/L_x\right)$ was produced. A kinematic viscosity $\nu = 10^{-2}$ was used, which corresponds to a Reynolds number $Re = UL_x/(2\nu) = 184$ on the basis of the half channel width and the root-mean-square velocity U. After a steady state is reached, the forcing is applied with $f = 0.38$ and $\omega = 2\pi/5$. Such parameters were chosen to provide close to maximum effect measured in terms of $\Pi_S^{(L)}/(2\nu\Omega)$, and they were kept fixed for all simulations while changing the value of θ_m. In all cases examined here, the resulting flow is periodic with the same periodicity of the local forcing (see the main text). The analysis was therefore performed over one period with the same code used for the experimental results. The final analysis was conducted in a 2 by 2 domain at the center of the simulation domain to obtain the results in Fig. 3, where local forcing was actively applied. For more intense forcing, nonperiodic (chaotic or turbulent) flows were observed, as well as solutions where periods longer than the pulsating period of the monopoles appeared. However, no such cases are presented here and they may be the object of future investigations.

Supplementary Materials

This PDF file includes:
Supplementary Text
Figs. S1 to S5

REFERENCES AND NOTES

1. A. N. Kolmogorov, The local structure of turbulence in incompressible viscous fluid for very large Reynolds numbers. *Dokl. Akad. Nauk SSSR* **30**, 301 (1941).
2. A. N. Kolmogorov, A refinement of previous hypotheses concerning the local structure of turbulence in a viscous incompressible fluid at high Reynolds number. *J. Fluid Mech.* **13**, 82–85 (1962).
3. R. H. Kraichnan, Inertial ranges in two-dimensional turbulence. *Phys. Fluids* **10**, 1417–1423 (1967).
4. S. B. Pope, *Turbulent Flows* (Cambridge Univ. Press, 2000). http://doi.org/10.1017/CBO9781316179475.
5. G. K. Batchelor, Computation of the energy spectrum in homogeneous two-dimensional turbulence. *Phys. Fluids* **12**, II-233–II-239 (1969).
6. L. F. Richardson, The supply of energy from and to atmospheric eddies. *Proc. R. Soc. Lond. A* **97**, 354–373 (1920).
7. H. Xia, D. Byrne, G. Falkovich, M. Shats, Upscale energy transfer in thick turbulent fluid layers. *Nat. Phys.* **7**, 321–324 (2011).
8. L. Fang, N. T. Ouellette, Multiple stages of decay in two-dimensional turbulence. *Phys. Fluids* **29**, 111105 (2017).
9. L. Fang, N. T. Ouellette, Spectral condensation in laboratory two-dimensional turbulence. *Phys. Rev. Fluids* **6**, 104605 (2021).
10. L. Fang, N. T. Ouellette, Advection and the efficiency of spectral energy transfer in two-dimensional turbulence. *Phys. Rev. Lett.* **117**, 104501 (2016).
11. Y. Liao, N. T. Ouellette, Geometry of scale-to-scale energy and enstrophy transport in two-dimensional flow. *Phys. Fluids* **26**, 045103 (2014).
12. X. Si, L. Fang, Interaction between swarming active matter and flow: The impact on Lagrangian coherent structures. *Phys. Rev. Fluids* **9**, 033101 (2024).
13. X. Si, L. Fang, Biologically generated turbulent energy flux in shear flow depends on tensor geometry. *PNAS Nexus* **3**, pgae056 (2024).
14. N. T. Ouellette, H. Xu, E. Bodenschatz, A quantitative study of three-dimensional Lagrangian particle tracking algorithms. *Exp. Fluids* **40**, 301–313 (2006).
15. J. P. Boyd, *Chebyshev and Fourier Spectral Methods* (Courier Corporation, 2001).
16. V. J. Valadão, G. Boffetta, M. Crialesi-Esposito, F. D. Lillo, S. Musacchio, Spectrum correction on Ekman-Navier-Stokes equation in two-dimensions. arXiv:2408.15735 (2024); https://doi.org/10.48550/arXiv.2408.15735.
17. X. SI, FangResearchGroup/Flow-Manipulation: 2025 Science Advances Manipulating 2D Turbulence (2025); https://doi.org/10.5281/zenodo.15571691.
18. A. N. Kolmogorov, Dissipation of energy in the locally isotropic turbulence. *Proc. R. Soc. Lond. A Math. Phys. Sci.* **434**, 15–17 (1991).
19. A. Alexakis, L. Biferale, Cascades and transitions in turbulent flows. *Phys. Rep.* **767-769**, 1–101 (2018).
20. R. T. Cerbus, P. Chakraborty, The third-order structure function in two dimensions: The Rashomon effect. *Phys. Fluids* **29**, 111110 (2017).
21. J. Weiss, The dynamics of enstrophy transfer in two-dimensional hydrodynamics. *Phys. D* **48**, 273–294 (1991).
22. S. Chen, R. E. Ecke, G. L. Eyink, M. Rivera, M. Wan, Z. Xiao, Physical mechanism of the two-dimensional inverse energy cascade. *Phys. Rev. Lett.* **96**, 084502 (2006).
23. A. D. Stroock, S. K. W. Dertinger, A. Ajdari, I. Mezić, H. A. Stone, G. M. Whitesides, Chaotic mixer for microchannels. *Science* **295**, 647–651 (2002).

24. H. A. Stone, A. D. Stroock, A. Ajdari, Engineering flows in small devices: Microfluidics toward a lab-on-a-chip. *Annu. Rev. Fluid Mech.* **36**, 381–411 (2004).
25. I. A. Houghton, J. R. Koseff, S. G. Monismith, J. O. Dabiri, Vertically migrating swimmers generate aggregation-scale eddies in a stratified column. *Nature* **556**, 497–500 (2018).
26. E. Kunze, J. F. Dower, I. Beveridge, R. Dewey, K. P. Bartlett, Observations of biologically generated turbulence in a coastal inlet. *Science* **313**, 1768–1770 (2006).
27. K. Katija, Biogenic inputs to ocean mixing. *J. Exp. Biol.* **215**, 1040–1049 (2012).
28. M. Olascoaga, I. I. Rypina, M. G. Brown, F. J. Beron-Vera, H. Koçak, L. E. Brand, G. R. Halliwell, L. K. Shay, Persistent transport barrier on the West Florida Shelf. *Geophys. Res. Lett.* **33**, L22603 (2006).
29. L. Fang, N. T. Ouellette, Influence of lateral boundaries on transport in quasi-two-dimensional flow. *Chaos* **28**, 023113 (2018).
30. W. K. Dewar, G. R. Flierl, Some effects of the wind on rings. *J. Phys. Oceanogr.* **17**, 1653–1667 (1987).
31. L. Renault, M. J. Molemaker, J. Gula, S. Masson, J. C. McWilliams, Control and stabilization of the Gulf Stream by oceanic current interaction with the atmosphere. *J. Phys. Oceanogr.* **46**, 3439–3453 (2016).
32. S. Rai, M. Hecht, M. Maltrud, H. Aluie, Scale of oceanic eddy killing by wind from global satellite observations. *Sci. Adv.* **7**, eabf4920 (2021).
33. M. Germano, Turbulence: The filtering approach. *J. Fluid Mech.* **238**, 325–336 (1992).
34. M. K. Rivera, W. B. Daniel, S. Y. Chen, R. E. Ecke, Energy and enstrophy transfer in decaying two-dimensional turbulence. *Phys. Rev. Lett.* **90**, 104502 (2003).
35. A. Leonard, Energy cascade in large-eddy simulations of turbulent fluid flows. *Adv. Geophys.* **18**, 237–248 (1975).
36. Y. Liao, N. T. Ouellette, Spatial structure of spectral transport in two-dimensional flow. *J. Fluid Mech.* **725**, 281–298 (2013).
37. J. G. Ballouz, N. T. Ouellette, Tensor geometry in the turbulent cascade. *J. Fluid Mech.* **835**, 1048–1064 (2018).
38. Z. Xiao, M. Wan, S. Chen, G. L. Eyink, Physical mechanism of the inverse energy cascade of two-dimensional turbulence: A numerical investigation. *J. Fluid Mech.* **619**, 1–44 (2009).
39. N. T. Ouellette, P. J. J. O'Malley, J. P. Gollub, Transport of finite-sized particles in chaotic flow. *Phys. Rev. Lett.* **101**, 174504 (2008).
40. D. Vella, L. Mahadevan, The "cheerios effect". *Am. J. Phys.* **73**, 817–825 (2005).
41. K. Schneider, M. Farge, Decaying two-dimensional turbulence in a circular container. *Phys. Rev. Lett.* **95**, 244502 (2005).

Acknowledgments

Funding: This work was supported by the US National Science Foundation under grant nos. CMMI-2143807 (to L.F.) and CBET-2429374 (to L.F.). **Author contributions:** L.F. conceived the original idea and supervised the project. X.S. ran the experiments and analyzed the data. G.B. and F.D.L. ran the simulation. All authors wrote the paper. **Competing interests:** The authors declare that they have no competing interests. **Data and materials availability:** All data needed to evaluate the conclusions in the paper are present in the paper and/or the Supplementary Materials. Data files and MATLAB scripts to reproduce the key figures are available at https://doi.org/10.5281/zenodo.15571691.

Submitted 4 December 2024
Accepted 18 June 2025
Published 25 July 2025
10.1126/sciadv.adv0956